



HAL
open science

Halobacillus ihumii sp. nov., a new bacterium isolated from stool of healthy children living in Mali

S. Konate, C.I. Lo, E. Kuete, M. Sarr, N. Amsrtong, A. Levasseur, A. Caputo, M.A. Thera, D. Raoult, M. Million

► **To cite this version:**

S. Konate, C.I. Lo, E. Kuete, M. Sarr, N. Amsrtong, et al.. Halobacillus ihumii sp. nov., a new bacterium isolated from stool of healthy children living in Mali. *New Microbes and New Infections*, 2020, 37, pp.100708. 10.1016/j.nmni.2020.100708 . hal-03150827

HAL Id: hal-03150827

<https://amu.hal.science/hal-03150827>

Submitted on 22 Aug 2022

HAL is a multi-disciplinary open access archive for the deposit and dissemination of scientific research documents, whether they are published or not. The documents may come from teaching and research institutions in France or abroad, or from public or private research centers.

L'archive ouverte pluridisciplinaire **HAL**, est destinée au dépôt et à la diffusion de documents scientifiques de niveau recherche, publiés ou non, émanant des établissements d'enseignement et de recherche français ou étrangers, des laboratoires publics ou privés.



Distributed under a Creative Commons Attribution - NonCommercial 4.0 International License

1 **PEGylation of Iron Doped Hydroxyapatite Nanoparticles for Increased Applicability as MRI**
2 **Contrast Agents and as Drug Vehicles: A study on Thrombogenicity, Cytocompatibility and Drug**
3 **Loading**

4 Tiago P. Ribeiro^{a,b}, Fernando J. Monteiro^{a,b,c}, Marta S. Laranjeira^{a,b,c,*}

5 ^ai3S-Instituto de Investigação e Inovação em Saúde, Universidade do Porto, Portugal

6 ^bINEB-Instituto de Engenharia Biomédica, Universidade do Porto, Portugal

7 ^cFEUP-Faculdade de Engenharia, DEMM, Universidade do Porto, Portugal

8

9

10

11

12

13

14

15

16

17

18

19

20 *** Corresponding author**

21 **Dr. Marta de Sousa Laranjeira**

22 **E-mail: mssl@ineb.up.pt**

23 **Tel: +351 220 408 800**

24 **PEGylation of Iron Doped Hydroxyapatite Nanoparticles for Increased Applicability as MRI**
25 **Contrast Agents and as Drug Vehicles: A study on Thrombogenicity, Cytocompatibility and Drug**
26 **Loading**

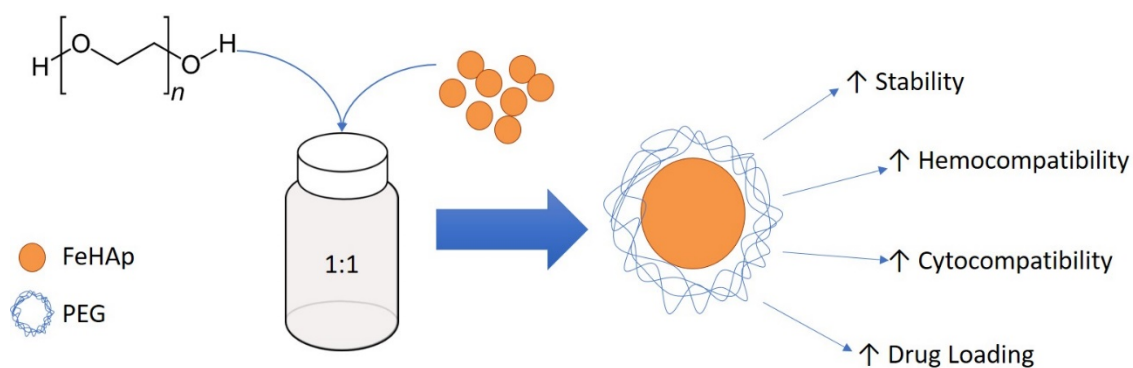
27 Tiago P. Ribeiro^{a,b}, Fernando J. Monteiro^{a,b,c}, Marta S. Laranjeira^{a,b,c,*}

28 ^aIS-Instituto de Investigação e Inovação em Saúde, Universidade do Porto, Portugal

29 ^bINEB-Instituto de Engenharia Biomédica, Universidade do Porto, Portugal

30 ^cFEUP-Faculdade de Engenharia, DEMM, Universidade do Porto, Portugal

31 **Graphical Abstract**



32

33

34

35

36

37

38

39 **Highlights**

- 40
- PEGylation enhances the biocompatibility of the nanoparticles
- 41
- PEG corrected the thrombogenic profile of the bare nanoparticles
- 42
- PEG molecular weight did not have a significant biological impact
- 43
- Higher molecular weight PEG increased drug loading

44 **Abstract**

45 Contrast agents are heavily used in order to increase the accuracy of imaging based diagnostic techniques
46 and since they are intravenously administrated, these agents need to be hemocompatible and
47 cytocompatible. This work is a follow-up of a previous study where iron doped hydroxyapatite
48 nanoparticles proved to increase contrast in MRI, however they were also highly thrombogenic when in
49 contact with blood. To overcome this drawback, a poly(ethylene glycol) coating was added to these
50 nanoparticles in order to increase hemocompatibility, cytocompatibility and act as a drug carrier, where
51 two different types of PEG were tested. After PEGylation, the PEG coating around the nanoparticles was
52 confirmed and quantified, comprising between 3 and 5% of the total mass of the particles. Furthermore,
53 both coated and non-coated particles were not hemolytical as already expected, however only the
54 PEGylated ones proved to be non-thrombogenic. Regarding cytocompatibility, at the end of 48h of
55 exposure only the PEGylated particles were non-cytotoxic, proving the relevance of the coating.
56 Additionally, the polymeric matrix was capable of increasing the nanoparticles drug loading capacity.
57 From all these results, it was possible to conclude that PEGylation of iron doped hydroxyapatite
58 nanoparticles provides a dual functionality, both increasing biocompatibility and drug loading.

59 **Keywords:** Biocompatibility; Drug loading; Magnetic hydroxyapatite; MRI contrast agents; PEG;
60 Surface modification

61

62 **1. Introduction**

63 Magnetic resonance imaging (MRI) is a very powerful tool for tumour detection, presenting a good
64 accuracy to safety ratio. Compared with other techniques, it has higher accuracy than ultrasounds, while
65 being safer than computer tomography since it uses electromagnetic radiation instead of ionizing
66 radiation.

67 Interestingly enough, for increased accuracy, these imaging techniques take advantage of certain
68 compounds that increase contrast, known as contrast agents. In MRI, the most common contrast agent is
69 gadoteric acid, which is a complex between a chelating agent and gadolinium(III), being heavily used for
70 shortening the T1 relaxation time [1]. However, despite being commonly and extensively used,
71 gadolinium is not naturally found in the human body, leading to high levels of toxicity, especially in

72 patients with poor kidney function that can develop a fatal condition known as nephrogenic system
73 fibrosis [2]. Knowing this, researchers shifted towards alternatives, such as magnetic iron-based
74 nanoparticles (NPs). These NPs are good substitutes, since iron is commonly found in the human body
75 and the small size of the particles allowed an easy administration [3]. One example of these are ferrite
76 NPs, which are superparamagnetic oxides and can reduce the T2 relaxation time, with products like
77 Feridex® and Combidex® being already developed [4]. To show this, Weng *et al.* made a comparison
78 between iron oxide nanoclusters and gadolinium based contrast agents, reporting an increased biosafety
79 profile of the iron oxide materials [5]. Yet, despite iron being safer than gadolinium, the high
80 concentration of iron and the low biodegradability of these magnetic NPs make them also connected with
81 bioaccumulation and toxicity [6]. To counteract these problems, magnetic hydroxyapatite (HAp) NPs are
82 proposed as a solution due to the high biocompatibility and biodegradability of HAp [7,8]. Several studies
83 have already proved that iron introduction into the structure of hydroxyapatite provides magnetic
84 properties to its usually non-magnetic behaviour [9–12]. Moreover, our previous studies showed that iron
85 doped hydroxyapatite (FeHAp) NPs can be used as contrast agents in MRI [9,13]. Therefore, combining
86 the magnetic behaviour, the low iron concentration and the degradability of these NPs, they should be
87 adequate to be used as safer MRI contrast agents.

88 Nevertheless, these nanosystems are usually intravenously administrated. In the blood system, they must
89 avoid deposition and aggregation, while being hemo- and cytocompatible for an appropriate mode of
90 action. In a previous study of ours, FeHAp NPs did not induce hemolysis, however they were highly
91 thrombogenic, which is a critical factor in intravenous administrated systems [13]. Thrombus formations
92 lead to clogged blood vessels and consequently, surface modification of NPs with biocompatible
93 polymers has been indicated for improved colloidal stability, hemocompatibility and lower toxicity. As an
94 example, a study made by Pinto *et al.* showed that the adsorption of polymers such as Polyethylene
95 Glycol (PEG) and Polyvinyl Alcohol (PVA) onto the surface of graphene platelets highly increased their
96 cytocompatibility and hemocompatibility [14]. In fact, PEG is one of the most studied biocompatible
97 polymers and due to its hydrophilic characteristic, it enables the modification of NPs in order to prevent
98 agglomeration, avoid protein adsorption and improve biocompatibility. With this thought, Lankveld *et al.*
99 compared bare gold NPs with PEGylated ones, concluding that the PEG modification induced higher
100 circulation times and made the NPs less prone to be uptake by the reticuloendothelial system, increasing
101 the NPs half-life inside the organism [15].

102 PEG can be covalently attached to some NPs or can also be non-covalently added. This last alternative
103 creates a matrix around the NPs which can act as a drug carrier as proven by León *et al.* [16]. Such
104 evidence is of major importance, since one of the main causes for chemotherapy low success rates is its
105 systemic action, versus which drug carriers purpose an enormous advantage. Drug carriers limit the
106 region of action, by transporting their contents to a specific region such as the tumour microenvironment.
107 Such feature enables not only a more efficient profile for the treatment but also the administration of
108 lower doses, ultimately leading to lower economic costs and systemic toxicity.

109 With this being explained, this work proposes the modification of FeHAp NPs surface with PEG using
110 PEG2000 and PEG8000, in order to avoid the thrombogenicity found in a previous work [13]. The
111 composites were also put into contact with fibroblasts for cytocompatibility assessment, and a
112 chemotherapeutical drug was introduced in order to create a drug carrier.

113

114 **2. Materials and Methods**

115 **2.1 Nanoparticles synthesis and PEGylation**

116 FeHAp NPs detailed production is described elsewhere [9]. Briefly, solutions of iron (III) nitrate (98+%,
117 Acros Organics, USA) and orthophosphoric acid (85 wt% solution in water, Acros Organics, USA) were
118 added dropwise into a previously heated to 100 °C, calcium hydroxide (98% extra pure, Acros Organics,
119 USA) solution. The pH was continuously measured and kept at 10 by adding ammonium hydroxide (25%
120 solution in water, Merck, Germany) as needed. After 2h of reaction, the particles were washed by
121 centrifugation with ultrapure water, dried at 60 °C and powdered. Finally, the NPs were sintered for 1h at
122 1000 °C with a heating rate of 5 °C min⁻¹ and stored in a desiccator for further use.

123 PEGylation of the NPs was performed in a non-covalent manner. With this purpose, 1% PEG2000
124 (Sigma-Aldrich, USA) and PEG8000 (Sigma-Aldrich, USA) solutions (w/v) were prepared separately, to
125 which FeHAp NPs were added in a 1:1 ratio. The mixture was stirred for 7h at room temperature, further
126 washed by centrifugation at 10 °C, dried under vacuum at room temperature and finally stored at 4 °C.
127 The PEG coated NPs were denominated PEG2 and PEG8 for PEG2000 and PEG8000, respectively.

128 **2.2 Physicochemical characterization of FeHAp and PEGylated NPs**

129 Morphological, atomic composition, **crystallographic studies and iron content** of FeHAp NPs were done
130 by transmission electron microscopy (TEM), energy-dispersive X-ray spectroscopy (EDX), X-ray
131 diffraction (XRD) **and Inductively Coupled Plasma-Atomic Emission Spectrometry (ICP-AES)**,
132 respectively. The results were already published and can be observed in the supplementary data on Fig.
133 **S1, Fig. S2 and Table S1** [9].

134 In order to confirm the formation of a PEG coating, Fourier Transform Infrared (FTIR) spectroscopy
135 analysis was carried out. Infrared spectra were recorded in a FTIR spectrometer (Perkin-Elmer, USA),
136 with a 4 cm^{-1} resolution and after an averaging of 32 scans per sample. Before analysis, pellets of KBr
137 were prepared by mixing 1 mg of the NPs with 200 mg of potassium bromide and compressed in a
138 hydraulic press (Grasedy Specac, USA). Pellets were produced in a low humidity environment for
139 improved sample quality.

140 **2.3 Thermogravimetric analysis**

141 The thermal behaviour of the FeHAp and PEGylated powders was studied by thermal gravimetric
142 analysis (TGA), using a NETZSCH STA 449F3 (NETZSCH, Germany). The thermal cycle, under
143 nitrogen atmosphere, started with a one-minute stage at 25°C followed by a $10\text{ }^{\circ}\text{C min}^{-1}$ slope up to 1000
144 $^{\circ}\text{C}$.

145 **2.4 Size distribution and Zeta Potential analysis**

146 Particle size, size distribution and zeta potential measurements were determined through dynamic light
147 scattering (DLS) in a Zetasizer Nano ZS (MALVERN, UK) with a scattering angle of 173° and a He-Ne
148 630 nm wavelength laser, using a Fraunhofer's model. For this, the dried particles were dispersed in
149 ultrapure water at a concentration of 1 mg mL^{-1} . Afterwards, the suspension was diluted 10 times in
150 ultrapure water before analysis. Three measurements were done per sample at $25\text{ }^{\circ}\text{C}$.

151 **2.5 Magnetic resonance imaging**

152 MRI experiments were performed with a 3T clinical scanner (Sigma HDXT 3T, GE Health Care, USA).
153 T2 contrast images were recorded by Sag T2 Fast Spin Eco technique with $\text{TR}=2500$, $\text{TE}=77,159$,
154 $\text{FOV}=240\text{ mm}$, eco train of 120, slices of 1 mm and a band width of 244 Hz. Samples were prepared by
155 dispersing the NPs in ultrapure water at a concentration of $500\text{ }\mu\text{g mL}^{-1}$. A water filled well was used as
156 the control group for qualitative analysis.

157 **2.6 Biological evaluation**

158 **2.6.1 Haemolysis assay**

159 Red blood cells were isolated from buffy coats (samples were obtained from Immuno-hemotherapy
160 Service, Hospital S. João, Porto, Portugal). Buffy coats were centrifuged at 4°C at 1500 rpm. The red
161 bottom layer was isolated and washed three times with PBS. The purified red blood cells were diluted to a
162 cell density of 2.0×10^8 cells mL⁻¹. 100 µL of the red blood cell suspension were added to a 96-well plate,
163 to which 100 µL of the NPs suspension were added. Incubation was carried for 3h at 37 °C at 80 rpm on
164 an orbital shaker. Afterwards, the suspensions were centrifuged at 1500 rpm for 15 minutes to collect the
165 supernatant. Finally, 80 µL were transferred to a 96-well black plate and absorbance was read at 540 nm
166 in a SynergyMX fluorimeter (BioTek, USA). The haemolysis percentage was calculated as follows:
167 Haemolysis (%) = (Hb value of sample/Hb of 100% haemolysis with 1% Triton X-100) x 100. The tested
168 NPs concentrations were 125, 250 and 500 µg mL⁻¹. Controls with PBS (negative control) and 1% Triton
169 X-100 (Sigma Aldrich, USA) in PBS (positive control for 100% haemolysis) were performed. All assays
170 were performed in triplicate.

171 **2.6.2 Thrombogenicity**

172 Thrombogenicity of the NPs was evaluated using the whole blood kinetic clotting time method. FeHAP
173 and PEGylated NPs, as well as positive (glass) and negative (polypropylene) controls, were used in a
174 concentration of 4000 µg mL⁻¹. Clotting reaction was activated with the addition of 100 µL of CaCl₂ (0.1
175 M) to each 1 mL of whole blood. Afterwards, 100 µL of the activated blood was put in contact with
176 controls and NPs for 5, 15, 25, 35 and 45 min. At the end of each time point, 3 mL of distilled water was
177 added and incubated for 5 min. The supernatant absorbance was measured at 540 nm, in a SynergyMX
178 fluorimeter (Biotek, USA). Red blood cells that were not trapped in a thrombus were lysed with addition
179 of distilled water (which causes complete haemolysis by hypoosmotic shock), thereby releasing
180 haemoglobin into water for subsequent measurement. The clot size is inversely proportional to the
181 absorbance value.

182 **2.6.3 Cytocompatibility**

183 Human gingival fibroblasts (HGF, ATCC, USA) were cultured in Alpha Modified Eagle Medium (α-
184 MEM, Gibco, Germany) supplemented with 10% (v/v) fetal bovine serum (FBS, Gibco, Germany) and

185 1% (v/v) penicillin/streptomycin (Biowest, France) and incubated at 37 °C and at 5% CO₂. Trypsinization
186 and seeding was performed every three days.

187 The metabolic activity of HGF, in contact with the PEGylated and bare FeHA_p NPs, was assessed by the
188 resazurin assay. Briefly, metabolically active cells can reduce the blue compound resazurin into resorufin,
189 turning it into a pink-purple appearance that can be detected by spectrophotometry [17]. For this assay,
190 the cells were trypsinized and seeded onto 96-well plates at a density of 5000 cells per well and incubated
191 for 24h. In parallel, the NPs were sterilized in ethanol, washed with sterile PBS and then re-dispersed in
192 complete supplemented α -MEM. After 24h of incubation, regular medium was exchanged for the
193 nanoparticle-rich medium, at concentrations of 125, 250 and 500 $\mu\text{g mL}^{-1}$, and the cells were again
194 incubated at 37 °C and at 5% CO₂. After 24h and 48h of incubation, each well was loaded with resazurin
195 (10% in α -MEM) and re-incubated for 4h. The medium was then transferred to a black 96-well plate and
196 fluorescence was measured at excitation and emission wavelengths of 566 and 605nm, respectively, in a
197 SynergyMX fluorimeter (BioTek, USA).

198 **2.7 Drug loading**

199 In this step all solutions were prepared in PBS pH=7.4. A 1 mg mL⁻¹ NPs suspension was added to 2 mL
200 of a 1 mg mL⁻¹ doxorubicin (98.0-102.0%, Sigma-Aldrich, Germany) solution and stirred at room
201 temperature in dark conditions for 24h. The suspension was then centrifuged (4000 rpm, 5 min) and the
202 supernatant and precipitate were separated. With this, the amount of drug loaded was determined as
203 follows: Drug loaded (%) = ((total amount of drug – drug in the supernatant) / total amount of drug) x
204 100.

205 **2.8 Statistical analysis**

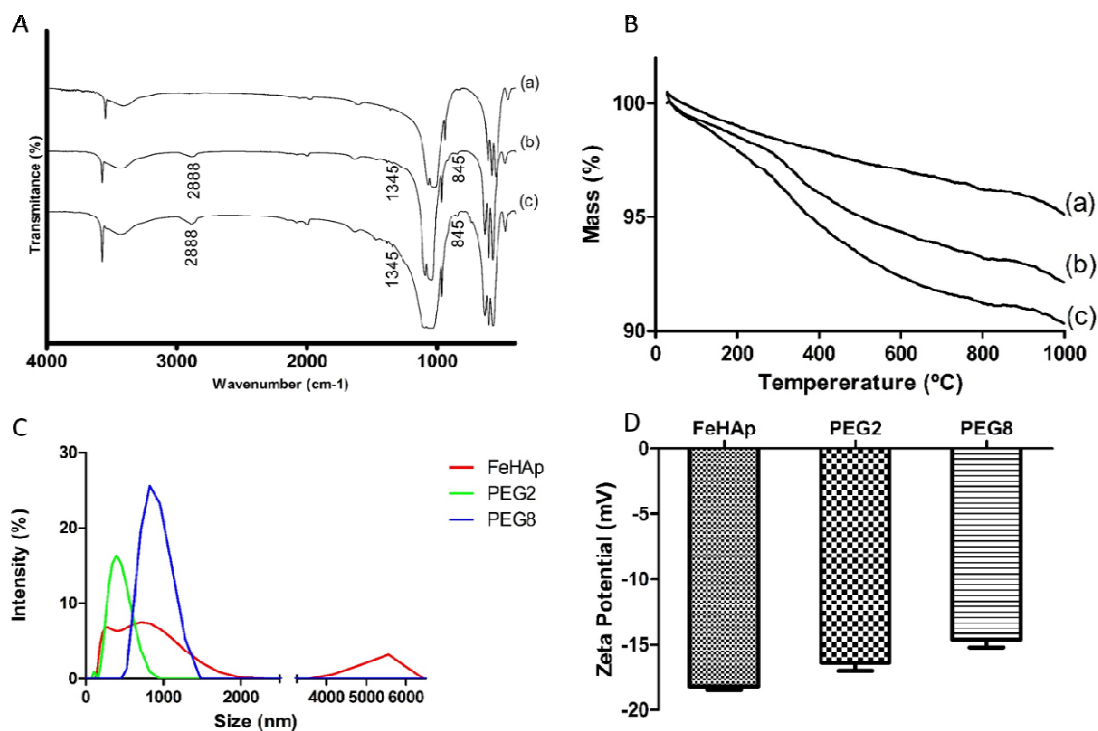
206 Statistical analysis and graphs were carried out with the GraphPad Prism 5 software (GraphPad, USA).
207 Data are represented as mean \pm standard deviation (SD). Statistical analysis was performed using the
208 analysis of variance One-way ANOVA, except for the thrombogenicity studies were a Two-way ANOVA
209 was employed, followed by Tukey's multiple comparison test, with n=3. Statistical significance was
210 considered when p<0.05 and represented with * for p<0.05, ** for p<0.01 and *** for p<0.001.

211

212 **3. Results**

213 **3.1 Physicochemical characterization**

214 The FTIR spectra, presented on Fig. 1A, shows that all samples comprised the characteristic peaks of
 215 HAp. Peaks corresponding to OH⁻ groups can be found at ~3572 cm⁻¹ and at 631 cm⁻¹. A broad band and
 216 a noticeable peak associated with adsorbed water are found at ~3436 cm⁻¹ and ~1630 cm⁻¹. Additionally,
 217 residual carbonates incorporated from atmospheric CO₂ can be found at ~877 cm⁻¹. Lastly, all four modes
 218 of PO₄³⁻ can be detected at ~960 cm⁻¹, ~475 cm⁻¹; ~1044 cm⁻¹, ~1090 cm⁻¹; ~570 cm⁻¹ and ~605 cm⁻¹.
 219 However, regarding the PEGylated NPs, PEG specific peaks can be detected at 845 cm⁻¹, 1345 cm⁻¹ and
 220 2888 cm⁻¹, which correspond to C-C, -CH and C-O stretching, respectively.



221 **Fig. 1.** Physicochemical characterization of the NPs. A) FTIR spectra of bare and PEGylated FeHAp NPs, a-FeHAp,
 222 b-PEG2, c-PEG8; B) Thermogravimetric analysis at and heating rate of 10 °C min⁻¹, a-FeHAp, b-PEG2, c-PEG8; C)
 223 Particle size distribution in water; D) Zeta potential analysis in water with the data being presented as mean ±
 224 standard deviation (n=3).
 225

226 On Fig. 1B is presented the thermogravimetric profile of the NPs. The presence of the polymer was
 227 confirmed due to the formation of a slope at ~300 °C that does not occur on the bare NPs, being attributed
 228 to polymer degradation. On the other hand, pristine FeHAp NPs presented little to no mass variation
 229 (~5% weight loss). Both the modified NPs lost, respectively for PEG2 and PEG8, 8% and 10% until 1000
 230 °C. Taking into the account the mass loss of pristine FeHAp Nps up to that temperature, it can be
 231 concluded that the total amount of polymer at the NPs surface was 3% and 5%, respectively for PEG2 and
 232 PEG8.

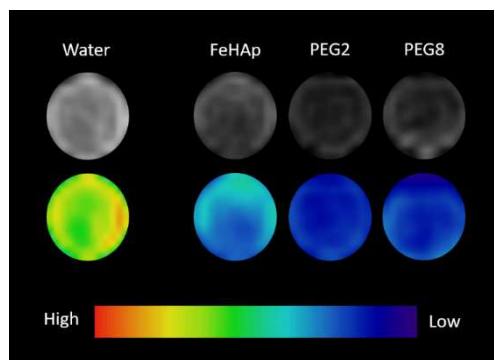


Fig. 2. T2-weighted MR images and the colour coded versions of bare and PEGylated FeHAp NPs at 500 $\mu\text{g mL}^{-1}$. The image of water was taken together for the purpose of comparison. In the colour coded image, high and low water intensities were indicated in red and blue, respectively.

233 Fig. 1C shows the particle size distribution of the NPs in water. For the bare FeHAp NPs three distinct
 234 populations were detected, one of them with sizes above 4000 nm which corresponds to particle
 235 aggregation. Dispersion after coating with PEG, drastically influenced the dispersion profile, creating one
 236 single population for each type of composite. Moreover, particles hydrodynamic size tended to increase
 237 when comparing PEG2 (approx. 435 nm) to PEG8 (approx. 875 nm).

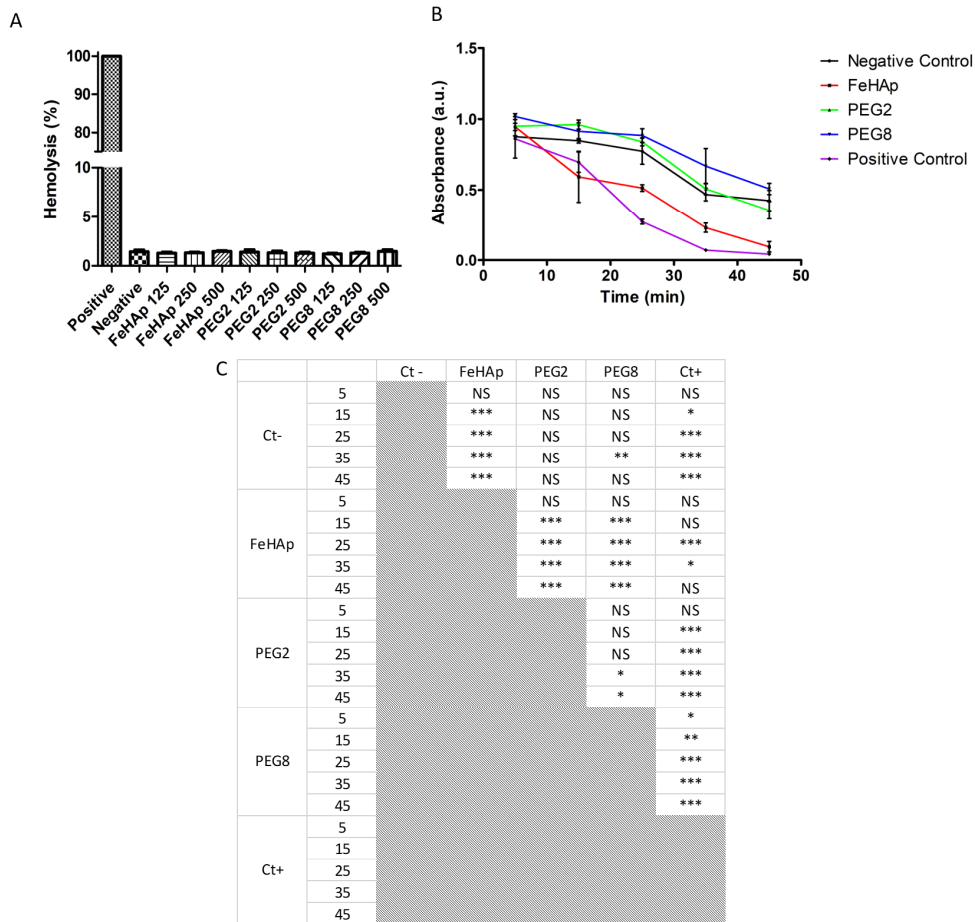
238 Regarding zeta potential analysis (Fig. 1D), the samples presented surface charges of $-18.2\text{mV} \pm 0.22$, -
 239 $16.37\text{mV} \pm 0.49$, $-14.63\text{mV} \pm 0.45$ for FeHAp, PEG2 and PEG8, respectively. The variation in surface
 240 charge also indicates the presence of adsorbed PEG.

241 3.2 MRI contrast potential

242 In Fig. 2 a T2-weighted MR image of the bare and PEGylated NPs dispersed in water may be observed. A
 243 brightness reduction was observed in comparison with water, clearly indicating the potential of these
 244 materials to serve as MRI contrast agents. Interestingly, PEGylation did not negatively impact the
 245 contrast potential of the bare FeHAp NPs, however the rapid deposition of the bare NPs induced a small
 246 decrease in the contrast potential when compared with the PEGylated ones.

247 3.2 Hemocompatibility analysis

248 As seen in Fig. 3A, all samples presented high hemocompatibility since the haemolysis percentage (<
 249 2%) of the test groups was very comparable with the negative control ($p > 0.05$). Additionally, no
 250 significant ($p > 0.05$) differences were observable between PEGylated and non-PEGylated NPs.



251

252 **Fig. 3.** Hemocompatibility assays. A) Hemolysis of red blood cells after 3h of incubation at 37 °C with PBS as the
 253 negative control, Triton X-100 as the positive control and several NP concentrations (125, 250 and 500 µg mL⁻¹). B)
 254 Measurement of whole blood kinetic clotting time for bare and PEGylated FeHAp NPs at a concentration of 4 mg
 255 mL⁻¹. The results are presented as mean ± standard deviation (n=3). C) Statistical analysis matrix of the
 256 thrombogenicity assay. * corresponds p<0.05, ** to p<0.01 and *** to p<0.001 while NS means non-significant.

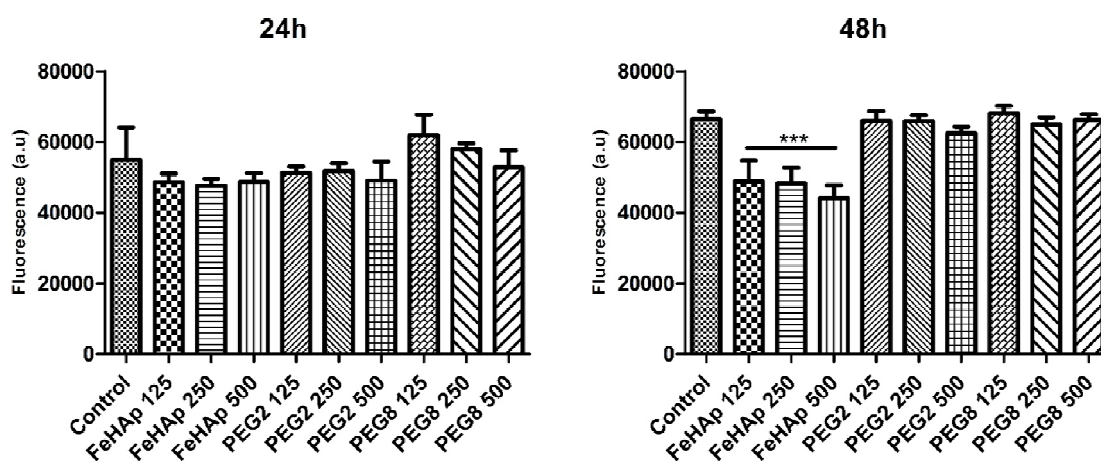


Fig. 4. Metabolic activity of HGF cells after 24h and 48h of incubation with bare and PEGylated FeHAp NPs at concentrations of 125, 250 and 500 $\mu\text{g mL}^{-1}$. *** correspond to $p < 0.001$ in comparison with the control group. Data are presented as mean \pm standard deviation ($n=3$).

257

258 3.3 Thrombogenicity evaluation

259 Fig. 3B presents the kinetics of the blood clotting process. Thrombus formation was evaluated for the
 260 PEGylated and bare NPs. In this assay, the size of the blood clot was inversely proportional to the
 261 absorbance level. Red blood cells trapped inside the thrombus are not lysed with the addition of distilled
 262 water (positive control), while the opposite occurs when no thrombus is formed (negative control). From
 263 the test, it was possible to confirm that FeHAp Nps were highly thrombogenic, close to the positive
 264 control ($p > 0.05$). However, the PEGylated samples corrected the problem, leading to less thrombus
 265 formation, being closer to the negative control ($p > 0.05$). Additionally, significant differences (Fig. 3C)
 266 were detected between the bare and the PEGylated samples, clearly indicating the influence of PEG in
 267 avoiding thrombus formations. Still, no significant differences were obtained when comparing PEG2 and
 268 PEG8 samples, suggesting that the chain length is not a factor during thrombus formation.

269

270

271

272

273

274 **3.4 Cytocompatibility evaluation**

275 The cytocompatibility of the produced NPs was confirmed with the resazurin assay. From Fig. 4, it was
276 possible to conclude that PEGylation increased the cytocompatibility of the NPs. In fact, after 24h the
277 bare NPs were biocompatible in comparison with the control group ($p>0.05$), however this profile
278 changed after 48h ($p<0.001$). It was also at this time point that PEGylation proved to be efficient in
279 reducing the toxicity, since the metabolic activity stayed high and very comparable to the control group
280 ($p>0.05$). Still, no significant differences ($p>0.05$) were detected between the different PEGylations with

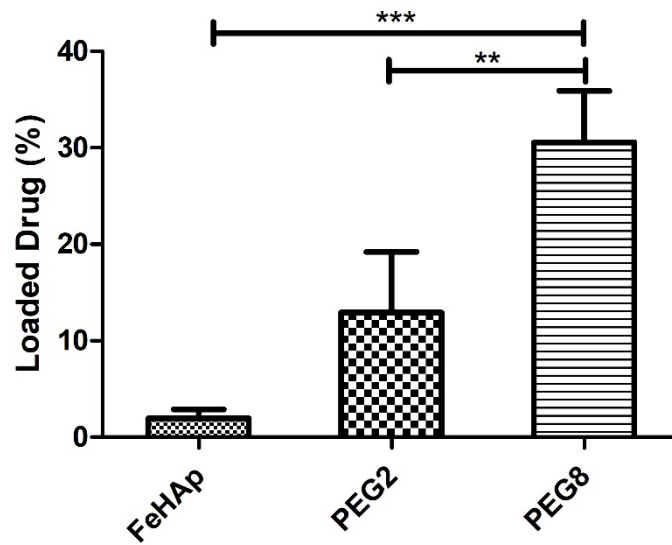


Fig. 5. Loaded drug into bare and PEGylated FeHAp NPs. ** corresponds to $p<0.01$ and *** to $p<0.001$. Data are presented as mean \pm standard deviation ($n=3$).

281 PEG2 and PEG8.

282 **3.5 Drug loading**

283 Fig. 5 shows the amount of loaded drug in the different NPs. The bare FeHAp NPs were able to carry a
284 small amount of drug ($1.96\% \pm 0.76$) however, the PEGylated NPs could carry a significant ($p<0.001$)
285 amount ($12.93\% \pm 5.14$) of drug with PEG8 being more efficient ($30.56\% \pm 4.37$) than PEG2 ($p<0.01$).

286

287 **4. Discussion**

288 To the best of our knowledge, the combination of FeHAp with PEG was never explored to date for *in*
289 *vitro* biological effects evaluation. The presence of the polymer at the surface of the FeHAp NPs was
290 confirmed through FTIR and quantified through TGA. FTIR is a technique that characterizes the

291 functional groups at the surface of materials and in the specific case of hydroxyapatite derived NPs, the
292 functional groups that can be detected are phosphate and hydroxyl groups, however with the presence of
293 PEG carbon associated groups, it was possible to confirm the presence of PEG at the surface of FeHAp
294 NPs [18]. Moreover, TGA is a useful technique to determine the presence of residual components in NPs.
295 This method is based on the observation of a mass loss in response to temperature increase. Since the
296 FeHAp NPs were sintered at 1000 °C no significant mass loss was detected, however on the PEGylated
297 NPs the abrupt mass loss at 300 °C was attributed to PEG degradation, confirming the presence of a PEG
298 layer on the NPs [19]. Comparing both PEG2 and PEG8 samples, the latest presented a higher mass loss,
299 which was expected due to the higher molecular weight of PEG 8000. In addition, the DLS analysis
300 indirectly confirmed the presence of the polymer due to zeta potential and size distribution variation.
301 Regarding the zeta potential analysis, FeHAp NPs usually present a negative surface charge at neutral pH,
302 due to the abundance of hydroxyl groups, which are also present in the terminal ends of PEG [20].
303 Despite the negative zeta potential of the PEGylated samples, the value tended to be less negative with
304 PEG chain size increase. We hypothesize that due to the non-covalent bonding of PEG, it masked the
305 negative charge of the bare NPs. In fact, Jiang et al. evaluated the zeta potential of chromium-doped zinc
306 gallate NPs before and after grafting PEG to the surface, concluding that the PEG modified NPs presented
307 a less negative zeta potential than the bare ones [21]. Moreover, as mentioned in section 1, NPs must
308 avoid aggregation and as confirmed by the size distribution, bare FeHAp NPs tend to form aggregates
309 (>4000 nm). Visually, after dispersion in water through sonication, the bare NPs formed visible
310 aggregates and tended to rapidly deposit at the bottom of the flasks. On the other hand, the PEGylated
311 samples formed a more stable suspension, being justified by the size distribution, which revealed a single
312 population of NPs. Such evidence, confirmed the potential of PEG in reducing the interactions between
313 NPs, and therefore avoid their aggregation and further deposition.

314 Despite being used for increased biocompatibility of magnetic NPs, polymer coating can alter their
315 magnetic response. FeHAp NPs are known for presenting a superparamagnetic behaviour which is a
316 required characteristic for MRI contrast [22]. From the obtained results their contrast potential is
317 confirmed due to the decreasing brightness. Additionally, the PEG coating provided a more uniform
318 contrast signal due to the increased stability of the NPs suspension, while the FeHAp NPs tended to
319 rapidly form aggregates and deposit, leading to an uneven signal.

320 Haemolysis in the presence of bare and PEGylated FeHAp NPs was very similar to the negative control,
321 proving to be non-haemolytic. The potential of NPs to harm erythrocytes derives from their
322 physicochemical characteristics (e.g. chemical composition, size, shape, surface charge). NPs with
323 sharper edges are more prone to damage erythrocytes, however the produced NPs have a slightly round
324 shape and the low haemolytic effects can derive from that [22,23]. Moreover, PEGylated NPs presented
325 very similar results ($p > 0.05$) to bare NPs, which was expected since PEG is known for increasing the
326 hemocompatibility of NPs, as shown by Ruan *et al.*, and therefore should not have any negative
327 contribution [24]. However, due to the lack of hemocompatibility studies on FeHAp NPs it is very
328 difficult to make comparisons, yet Yildirim *et al.* studied the hemocompatibility of mesoporous silica NPs
329 and obtained very similar results regarding the haemolytical activity. In that study, it was reported that
330 there is no correlation between surface charge and haemolysis, being the exposed functional hydroxyl
331 groups responsible for interacting with red blood cells membrane and induce damage [25]. In the case of
332 FeHAp NPs, there are also hydroxyl groups at the surface, meaning that FeHAp NPs should prove
333 haemolytical, However, these amount of exposed hydroxyl groups may not be sufficient to induce cell
334 membrane damage. In fact, Lin *et al.* reported that mesoporous silica NPs were significantly less
335 haemolytical than non-porous silica NPs, justifying this occurrence with the amount of exposed hydroxyl
336 groups [26].

337 These blood interaction results mimic those obtained in a previous work, where the main problem was
338 thrombus formation [13]. Fortunately, from the obtained results, PEGylation solved this problem.
339 Thrombus formation is the last product from the activation of the coagulation cascade [27]. The high
340 thrombogenicity of FeHAp NPs is directly linked to the trivalent characteristic of Fe^{3+} ions. These ions
341 easily react with hydroxyl groups of water and produce powerful hydroxyl radicals. Furthermore, these
342 radicals are the most biologically damaging ones and when in contact with blood increase the formation
343 of blood clots, deriving from the conversion of soluble fibrinogen into fibrin-like polymers [28]. It is
344 possible that Fe^{3+} ions are released from the NPs and that those are sufficient to start the clotting process.
345 However, PEG serves as a protective layer around the NPs, ultimately leading to less interaction with
346 biological fluids and therefore reducing the release of iron ions, which could explain the non-
347 thrombogenic behaviour of the PEGylated NPs in comparison with their bare counterparts [29]. It is also
348 important to notice that in this study a high concentration of NPs (4 mg mL^{-1}) was tested, being higher

349 than the usual dose of intravenously administrated contrast agents (50 mg Kg^{-1}) which roughly
350 correspond to 0.5 mg mL^{-1} , clearly indicating their capability for being intravenously administrated [25].

351 Additionally, due to Fe^{3+} and Ca^{2+} ions release, FeHAp NPs proved to be toxic to cells after 48h. It is
352 known that Ca^{2+} ions are released from hydroxyapatite NPs during the degradation process that occurs
353 both intracellularly and extracellularly [30]. In the case of FeHAp, both Fe^{3+} and Ca^{2+} ions are expected to
354 be released, leading to ion imbalances than can disrupt cellular mechanisms [22]. Ca^{2+} excess is usually
355 associated with mitochondrial damage and activation of an apoptotic response in cancer cells, however on
356 healthy cells such overload is quickly counterbalanced in order to avoid toxicity [30,31]. On the other
357 hand, Fe^{3+} is related with reactive oxygen species (ROS) production usually via the Fenton reaction,
358 which leads to the formation of hydroxyl radicals [32]. From the obtained results, since bare FeHAp NPs
359 did not induce toxic effects after 24h, it was hypothesized that it is derived from the low degree of
360 degradation and therefore low ions release. However, after 48h a significant decrease in the metabolic
361 activity was detected, showing the toxic profile of the bare FeHAp NPs, which is probably derived from
362 the release of Fe^{3+} ions. However, the PEGylated NPs did not impact the cell metabolic activity at 48h of
363 exposure, which could be explained by lower cellular internalization and delayed degradation, since PEG
364 produces a protective layer around the NPs, limiting their direct contact with biological fluids [29].

365 Finally, regarding the drug loading experiments, PEGylation induced higher drug uptake. Hydroxyapatite
366 NPs have already been explored as drug carriers, especially due to their high biocompatibility [33,34]. In
367 this case, it was observed a slight level of drug adsorption on the bare FeHAp NPs was observed,
368 probably due to interactions between the negative surface charge of the NPs and the positively-charged
369 amine moiety of doxorubicin. More interestingly, due to the polymer matrix on the PEGylated samples,
370 the loaded drug percentage increased significantly, **which may be explained through charge interactions**
371 **and hydrogen bonding**. Additionally, when comparing both PEGylated samples, PEG8 showed increased
372 drug loading, which may be explained by the longer chains of PEG, that contributed to the matrix size
373 increase.

374

375 **5. Conclusions**

376 This work describes an easy solution for increasing the biocompatibility of FeHAp NPs, while creating a
377 drug carrier for cytostatic drugs with potential application in some cancers. The PEG modified surfaces

378 successfully decreased the NPs agglomeration, avoided their high thrombogenic profile up to 4 mg mL⁻¹,
379 increased their cytocompatibility up to 48h with concentrations as high as 500 µg mL⁻¹ and even
380 increased the amount of loaded drug. It is important to emphasize that between PEG2000 and PEG8000
381 no significant differences were detected on the biologic assays, meaning that the choice between both
382 polymers only varies depending on the amount of drug that is intended to be loaded. Therefore,
383 PEGylation is in fact an easy method to provide all the necessary conditions for FeHAp NPs to be used as
384 a blood administered MRI contrast agent that could also carry a drug for a complementary therapeutic
385 effect. Additionally, due to the simplicity of the proposed PEGylation method, it can be expanded to
386 several other types of NPs, increasing their biological applicability.

387

388

389

390

391

392

393

394

395

396

397

398

399

400

401

402

403 **Acknowledgements**

404 The authors acknowledge project Biotherapies (NORTE-01-0145-FEDER-000012), supported by Norte
405 Portugal Regional Operational Program (NORTE2020), under the PORTUGAL 2020 Partnership
406 Agreement, through the European Regional Development Fund (ERDF). This work was also financed by
407 FEDER - Fundo Europeu de Desenvolvimento Regional funds through the COMPETE 2020 -
408 Operational Programme for Competitiveness and Internationalization (POCI), PORTUGAL 2020, in the
409 framework of the project “Institute for Research and Innovation in Health Sciences”(POCI-01-0145-
410 FEDER-00727). The authors also acknowledge the support of the i3S Scientific Platform Biointerfaces
411 and Nanotechnology (UID/BIM/04293/2019). Additionally, the authors acknowledge the collaboration of
412 João A. M. Santos and Pedro Conde from the Medical Physics, Radiobiology and Radiation Protection
413 Group, IPO Porto Research Center (CI-IPOP), Portuguese Oncology Institute of Porto (IPO Porto), Porto,
414 Portugal, during MRI image acquisition.

415

416

417

418

419

420

421

422

423

424

425

426

427

428 **References**

- 429 [1] J. Wahsner, E.M. Gale, A. Rodríguez-Rodríguez, P. Caravan, Chemistry of MRI contrast agents:
430 Current challenges and new frontiers, *Chem. Rev.* 119 (2019) 957–1057.
431 <https://doi.org/10.1021/acs.chemrev.8b00363>.
- 432 [2] R.C. Semelka, J.P. Prybylski, M. Ramalho, Influence of excess ligand on Nephrogenic Systemic
433 Fibrosis associated with nonionic, linear gadolinium-based contrast agents, *Magn. Reson.*
434 *Imaging.* 58 (2019) 174–178. <https://doi.org/10.1016/j.mri.2018.11.015>.
- 435 [3] H. Wei, O.T. Bruns, M.G. Kaul, E.C. Hansen, M. Barch, A. Wiśniowska, O. Chen, Y. Chen, N.
436 Li, S. Okada, J.M. Cordero, M. Heine, C.T. Farrar, D.M. Montana, G. Adam, H. Ittrich, A.
437 Jasanoff, P. Nielsen, M.G. Bawendi, Exceedingly small iron oxide nanoparticles as positive MRI
438 contrast agents, *Proc. Natl. Acad. Sci. U. S. A.* 114 (2017) 2325–2330.
439 <https://doi.org/10.1073/pnas.1620145114>.
- 440 [4] M.A. Miller, S. Arlauckas, R. Weissleder, Prediction of anti-cancer nanotherapy efficacy by
441 imaging, *Nanotheranostics.* 1 (2017) 296–312. <https://doi.org/10.7150/ntno.20564>.
- 442 [5] Q. Weng, X. Hu, J. Zheng, F. Xia, N. Wang, H. Liao, Y. Liu, D. Kim, J. Liu, F. Li, Q. He, B.
443 Yang, C. Chen, T. Hyeon, D. Ling, Toxicological Risk Assessments of Iron Oxide Nanocluster-
444 and Gadolinium-Based T1MRI Contrast Agents in Renal Failure Rats, *ACS Nano.* 13 (2019)
445 6801–6812. <https://doi.org/10.1021/acsnano.9b01511>.
- 446 [6] H. Ittrich, K. Peldschus, N. Raabe, M. Kaul, G. Adam, Superparamagnetic iron oxide
447 nanoparticles in biomedicine: Applications and developments in diagnostics and therapy, *RoFo*
448 *Fortschritte Auf Dem Gebiet Der Rontgenstrahlen Und Der Bildgeb. Verfahren.* 185 (2013)
449 1149–1166. <https://doi.org/10.1055/s-0033-1335438>.
- 450 [7] J. Barros, M.P. Ferraz, J. Azeredo, M.H. Fernandes, P.S. Gomes, F.J. Monteiro, Alginate-
451 nanohydroxyapatite hydrogel system: Optimizing the formulation for enhanced bone
452 regeneration, *Mater. Sci. Eng. C.* 105 (2019) 109985.
453 <https://doi.org/10.1016/j.msec.2019.109985>.
- 454 [8] P. Turon, L. del Valle, C. Alemán, J. Puiggali, Biodegradable and Biocompatible Systems Based
455 on Hydroxyapatite Nanoparticles, *Appl. Sci.* 7 (2017) 60. <https://doi.org/10.3390/app7010060>.

- 456 [9] T.P. Ribeiro, F.J. Monteiro, M.S. Laranjeira, Duality of iron (III) doped nano hydroxyapatite in
457 triple negative breast cancer monitoring and as a drug-free therapeutic agent, *Ceram. Int.* 46
458 (2020) 16590–16597. <https://doi.org/10.1016/j.ceramint.2020.03.231>.
- 459 [10] A. Tampieri, T. D'Alessandro, M. Sandri, S. Sprio, E. Landi, L. Bertinetti, S. Panseri, G.
460 Peponi, J. Goettlicher, M. Bañobre-López, J. Rivas, Intrinsic magnetism and hyperthermia in
461 bioactive Fe-doped hydroxyapatite, *Acta Biomater.* 8 (2012) 843–851.
462 <https://doi.org/10.1016/j.actbio.2011.09.032>.
- 463 [11] D.F. Mercado, G. Magnacca, M. Malandrino, A. Rubert, E. Montoneri, L. Celi, A. Bianco Prevot,
464 M.C. Gonzalez, Paramagnetic iron-doped hydroxyapatite nanoparticles with improved metal
465 sorption properties. A bioorganic substrates-mediated synthesis, *ACS Appl. Mater. Interfaces.* 6
466 (2014) 3937–3946. <https://doi.org/10.1021/am405217j>.
- 467 [12] A. Gloria, T. Russo, U. D'Amora, S. Zeppetelli, T. D'Alessandro, M. Sandri, M. Banobre-Lopez,
468 Y. Pineiro-Redondo, M. Uhlarz, A. Tampieri, J. Rivas, T. Herrmannsdorfer, V.A. Dediu, L.
469 Ambrosio, R. De Santis, Magnetic poly(-caprolactone)/iron-doped hydroxyapatite
470 nanocomposite substrates for advanced bone tissue engineering, *J. R. Soc. Interface.* 10 (2013)
471 20120833–20120833. <https://doi.org/10.1098/rsif.2012.0833>.
- 472 [13] M.S. Laranjeira, A. Moço, J. Ferreira, S. Coimbra, E. Costa, A. Santos-Silva, P.J. Ferreira, F.J.
473 Monteiro, Different hydroxyapatite magnetic nanoparticles for medical imaging: Its effects on
474 hemostatic, hemolytic activity and cellular cytotoxicity, *Colloids Surfaces B Biointerfaces.* 146
475 (2016) 363–374. <https://doi.org/10.1016/j.colsurfb.2016.06.042>.
- 476 [14] A.M. Pinto, J.A. Moreira, F.D. Magalhães, I.C. Gonçalves, Polymer surface adsorption as a
477 strategy to improve the biocompatibility of graphene nanoplatelets, *Colloids Surfaces B*
478 *Biointerfaces.* 146 (2016) 818–824. <https://doi.org/10.1016/j.colsurfb.2016.07.031>.
- 479 [15] D.P. Lankveld, R.G. Rayavarapu, P. Krystek, A.G. Oomen, H.W. Verharen, T.G. van Leeuwen,
480 W.H. De Jong, S. Manohar, Blood clearance and tissue distribution of PEGylated and non-
481 PEGylated gold nanorods after intravenous administration in rats, *Nanomedicine.* 6 (2011) 339–
482 349. <https://doi.org/10.2217/nmm.10.122>.
- 483 [16] A. León, P. Reuquen, C. Garín, R. Segura, P. Vargas, P. Zapata, P.A. Orihuela, FTIR and raman

484 characterization of TiO₂ nanoparticles coated with polyethylene glycol as carrier for 2-
485 methoxyestradiol, *Appl. Sci.* 7 (2017) 1–9. <https://doi.org/10.3390/app7010049>.

486 [17] C.C. Coelho, S.R. Sousa, F.J. Monteiro, Heparinized nanohydroxyapatite/collagen granules for
487 controlled release of vancomycin, *J. Biomed. Mater. Res. - Part A.* 103 (2015) 3128–3138.
488 <https://doi.org/10.1002/jbm.a.35454>.

489 [18] C.C. Coelho, R. Araújo, P.A. Quadros, S.R. Sousa, F.J. Monteiro, Antibacterial bone substitute of
490 hydroxyapatite and magnesium oxide to prevent dental and orthopaedic infections, *Mater. Sci.*
491 *Eng. C.* 97 (2019) 529–538. <https://doi.org/10.1016/j.msec.2018.12.059>.

492 [19] H.J. Parab, J.H. Huang, T.C. Lai, Y.H. Jan, R.S. Liu, J.L. Wang, M. Hsiao, C.H. Chen, Y.K.
493 Hwu, D.P. Tsai, S.Y. Chuang, J.H.S. Pang, Biocompatible transferrin-conjugated sodium
494 hexametaphosphate-stabilized gold nanoparticles: Synthesis, characterization, cytotoxicity and
495 cellular uptake, *Nanotechnology.* 22 (2011). <https://doi.org/10.1088/0957-4484/22/39/395706>.

496 [20] M. Iafisco, M. Sandri, S. Panseri, J.M. Delgado-López, J. Gómez-Morales, A. Tampieri,
497 Magnetic bioactive and biodegradable hollow Fe-doped hydroxyapatite coated poly(L-lactic) acid
498 micro-nanospheres, *Chem. Mater.* 25 (2013) 2610–2617. <https://doi.org/10.1021/cm4007298>.

499 [21] Y. Jiang, Y. Li, C. Richard, D. Scherman, Y. Liu, Hemocompatibility investigation and
500 improvement of near-infrared persistent luminescent nanoparticle ZnGa₂O₄:Cr³⁺ by surface
501 PEGylation, *J. Mater. Chem. B.* 7 (2019) 3796–3803. <https://doi.org/10.1039/c9tb00378a>.

502 [22] T.P. Ribeiro, F.J. Monteiro, M.S. Laranjeira, Duality of iron (III) doped nano hydroxyapatite in
503 triple negative breast cancer monitoring and as a drug-free therapeutic agent, *Ceram. Int.* (2020).
504 <https://doi.org/10.1016/j.ceramint.2020.03.231>.

505 [23] A.M. Pinto, C. Gonçalves, D.M. Sousa, A.R. Ferreira, J.A. Moreira, I.C. Gonçalves, F.D.
506 Magalhães, Smaller particle size and higher oxidation improves biocompatibility of graphene-
507 based materials, *Carbon N. Y.* 99 (2016) 318–329. <https://doi.org/10.1016/j.carbon.2015.11.076>.

508 [24] S. Ruan, J. Wan, Y. Fu, K. Han, X. Li, J. Chen, Q. Zhang, S. Shen, Q. He, H. Gao, PEGylated
509 fluorescent carbon nanoparticles for noninvasive heart imaging, *Bioconjug. Chem.* 25 (2014)
510 1061–1068. <https://doi.org/10.1021/bc5001627>.

- 511 [25] A. Yildirim, E. Ozgur, M. Bayindir, Impact of mesoporous silica nanoparticle surface
512 functionality on hemolytic activity, thrombogenicity and non-specific protein adsorption, *J.*
513 *Mater. Chem. B.* 1 (2013) 1909–1920. <https://doi.org/10.1039/c3tb20139b>.
- 514 [26] Y.S. Lin, C.L. Haynes, CH₂-Hemolysis and size different MSN, *J. Am. Chem. Soc.* 132 (2010)
515 4834–4842. <https://doi.org/10.1021/ja910846q>.
- 516 [27] G. Lippi, M. Franchini, G. Targher, Arterial thrombus formation in cardiovascular disease, *Nat.*
517 *Rev. Cardiol.* 8 (2011) 502–512. <https://doi.org/10.1038/nrcardio.2011.91>.
- 518 [28] B. Lipinski, E. Pretorius, H.M. Oberholzer, W.J. van der Spuy, Interaction of Fibrin with Red
519 Blood Cells: The Role of Iron, *Ultrastruct. Pathol.* 36 (2012) 79–84.
520 <https://doi.org/10.3109/01913123.2011.627491>.
- 521 [29] V. Cauda, A. Schlossbauer, T. Bein, Bio-degradation study of colloidal mesoporous silica
522 nanoparticles: Effect of surface functionalization with organo-silanes and poly(ethylene glycol),
523 *Microporous Mesoporous Mater.* 132 (2010) 60–71.
524 <https://doi.org/10.1016/j.micromeso.2009.11.015>.
- 525 [30] R. Meena, K.K. Kesari, M. Rani, R. Paulraj, Effects of hydroxyapatite nanoparticles on
526 proliferation and apoptosis of human breast cancer cells (MCF-7), *J. Nanoparticle Res.* 14 (2012).
527 <https://doi.org/10.1007/s11051-011-0712-5>.
- 528 [31] Y. Han, S. Li, X. Cao, L. Yuan, Y. Wang, Y. Yin, T. Qiu, H. Dai, X. Wang, Different inhibitory
529 effect and mechanism of hydroxyapatite nanoparticles on normal cells and cancer cells in vitro
530 and in vivo, *Sci. Rep.* 4 (2014) 1–8. <https://doi.org/10.1038/srep07134>.
- 531 [32] Z. Shen, T. Liu, Y. Li, J. Lau, Z. Yang, W. Fan, Z. Zhou, C. Shi, C. Ke, V.I. Bregadze, S.K.
532 Mandal, Y. Liu, Z. Li, T. Xue, G. Zhu, J. Munasinghe, G. Niu, A. Wu, X. Chen, Fenton-
533 Reaction-Acceleratable Magnetic Nanoparticles for Ferroptosis Therapy of Orthotopic Brain
534 Tumors, *ACS Nano.* 12 (2018) 11355–11365. <https://doi.org/10.1021/acsnano.8b06201>.
- 535 [33] S.C. Thomas, H. Sharma, P. Rawat, A.K. Verma, A. Leekha, V. Kumar, A. Tyagi, B.S. Gurjar, Z.
536 Iqbal, S. Talegaonkar, Synergistic anticancer efficacy of Bendamustine Hydrochloride loaded
537 bioactive Hydroxyapatite nanoparticles: In-vitro, ex-vivo and in-vivo evaluation, *Colloids*
538 *Surfaces B Biointerfaces.* 146 (2016) 852–860. <https://doi.org/10.1016/j.colsurfb.2016.07.035>.

539 [34] Y. Zhang, L. Zhang, Q. Ban, J. Li, C.H. Li, Y.Q. Guan, Preparation and characterization of
540 hydroxyapatite nanoparticles carrying insulin and gallic acid for insulin oral delivery,
541 Nanomedicine Nanotechnology, Biol. Med. 14 (2018) 353–364.
542 <https://doi.org/10.1016/j.nano.2017.11.012>.

543

544

545

546

547

548

549

550

551

552

553

554

555

556

557

558

559

560

561